

Temperature evolution of the helical magnetic structure in the metallic Kagome system YMn_6Sn_6

Rebecca Dally

NIST Center for Neutron Research, National Inst. Standards and Technology, 100 Bureau Drive, Gaithersburg, MD 20899

Updated: September 26, 2022

Software requirements: DAVE (<https://www.ncnr.nist.gov/dave/download.html>)

Abstract

This experiment will demonstrate the versatility of triple-axis spectrometers for diffraction experiments and the application to particularly topical materials, namely, YMn_6Sn_6 . YMn_6Sn_6 is a metallic Kagome system, which has a zero-applied magnetic field antiferromagnetic transition at 345 K to a commensurate structure with wavevector $\mathbf{k} = (0, 0, \frac{1}{2})$. This commensurate structure is short lived and quickly transitions to a double-flat helical magnetic structure. This helix propagates incommensurately with the c -axis in this hexagonal structure and the pitch length varies from about two unit cells to almost four between its onset at 333 K to the base temperature measured (12 K). There is an additional complexity in this system, which is that two separate helical structures exist simultaneously with similar wavevectors. Here, experimenters will learn how to set-up experiments on a TAS which will include how to mount and align a sample. Data collection will include the observation of the magnetic peaks in YMn_6Sn_6 and tracking the temperature dependence. Analysis will include data reduction, plotting, and fitting of the data to quantify the zero-field properties described. The data used for this experiment helped lead to the publications in Refs. [1] and [2], and the experiments were performed on the thermal triple-axis spectrometer, BT-7 [3], at the NIST Center for Neutron Research.

Triple-axis spectrometer basics

A triple-axis spectrometer (TAS) is an extremely versatile instrument for studying the static and/or dynamic structure from single-crystal, polycrystalline, thin-film, and even amorphous samples. The three axes refer to the monochromator scattering angle ($2\theta_M$), sample scattering angle ($2\theta_S$), and analyzer scattering angle ($2\theta_A$) which

1. neutron beam
2. collimator
3. monochromator
4. sample
5. analyzer
6. detector

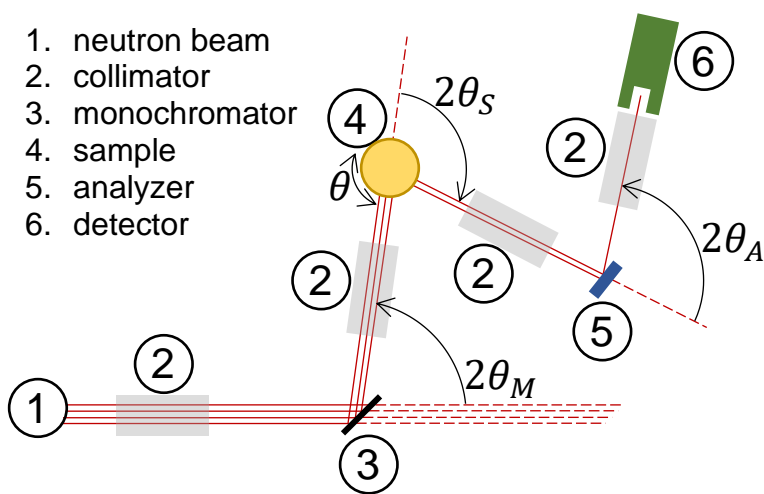


Fig. 1 A top-down view of a triple-axis spectrometer layout.

allow the user to control the incident energy, Q -value, and detected final energy, respectively (Fig. 1). Control of the resolution, both in momentum and energy, can be customized through collimators and various focusing modes of the monochromator and analyzer. Coarser resolution results in greater flux and finer resolution leads to less flux, and the user must weigh the value and trade-offs in deciding what configuration route to take. Most TASs have a large sample area which can accommodate a variety of sample environments including closed-cycle cryostats (CCRs), dilution refrigerators, furnaces, and superconducting magnets.

TASs are known for having excellent signal-to-noise and momentum resolution. Thermal TAS instruments, like BT-7, have good energy resolution (~ 0.1 meV FWHM or better at the elastic line) and energy transfer ranges (*e.g.* BT-7 incident energies range between ~ 5 meV to 500 meV), whereas cold TAS instruments are known for exceptional energy resolution albeit a more limited (Q , E) range due to the longer wavelength/lower energy neutrons. Typically the TAS explores a two-dimensional reciprocal space plane¹ (*e.g.* $(H, K, 0)$, $(H, 0, L)$, or (H, H, L)),

¹ There are 2D detectors that can be used with TASs which cover a limited number of degrees out of the scattering plane

in studying phase transitions, critical phenomena, superconductors, magnons, phonons, and much more.

Many TAS instruments are also constructed to accommodate polarized neutron experiments. Polarized neutrons can discriminate between nuclear and magnetic scattering and can give information about the direction of magnetic moments and fluctuations. BT-7 can be configured for polarization analysis. [4, 5]

Alignment

An important consideration when planning a TAS experiment is deciding the scattering plane in which the sample will be oriented. For planning this experiment, we had prior knowledge that the magnetic wavevector that we wanted to study was $\mathbf{k} = (0, 0, k_z)$; the scattering plane we chose had to then include L , such as $(H, 0, L)$ or (H, H, L) . It's always a good idea to map out the relationship between a single crystals' direct space axes and reciprocal space axes to understand how the physical placement of your crystal on the instrument will lead to scattering from the desired reciprocal space plane. This is more important for space groups with non-90° angles where the direct space axes and reciprocal space axes are non-parallel (*e.g.* see Fig. 2a, b).

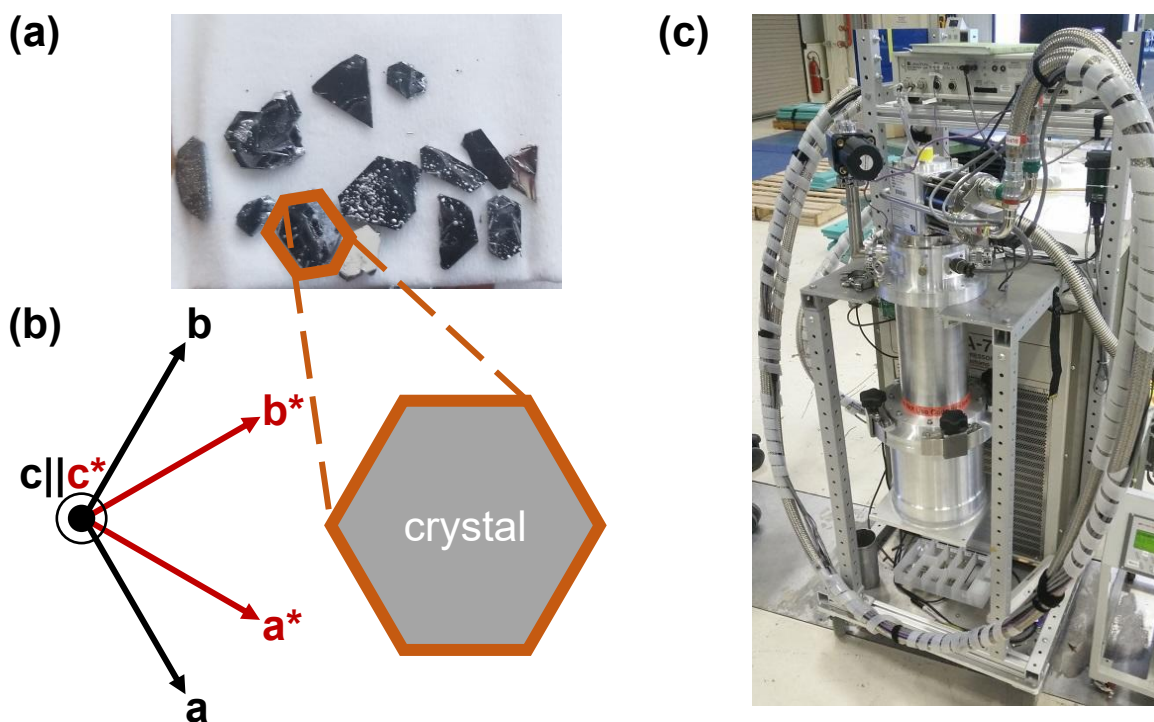


Fig. 2 (a) Single-crystals of YMn_6Sn_6 . (b) A schematic of the direct space lattice vectors and reciprocal space lattice vectors with respect to the crystal shape. (c) The high-temperature, high-power cryostat (14 K – 800 K) used in this experiment. Sample was loaded via the bottom of the cryostat such that the scattering plane was $(H, 0, L)$.

Picking the appropriate TAS configuration

Ref. [3] contains a thorough synopsis of the different operating modes for BT-7 and the appropriate times for when to use each. Below is a short summary of some options on BT-7.

- Collimation: BT-7 has four Söller slit collimator (Figs. 1 and 3b) positions located before the monochromator (in-pile), before the sample, after the sample, and before the detector. The number on the collimator is in arc minutes ($'$) and describes the FWHM of the divergence of a neutron beam after passing through it. BT-7 can also accommodate radial collimators before and after the analyzer. The choice of collimation will determine the momentum and energy resolution.

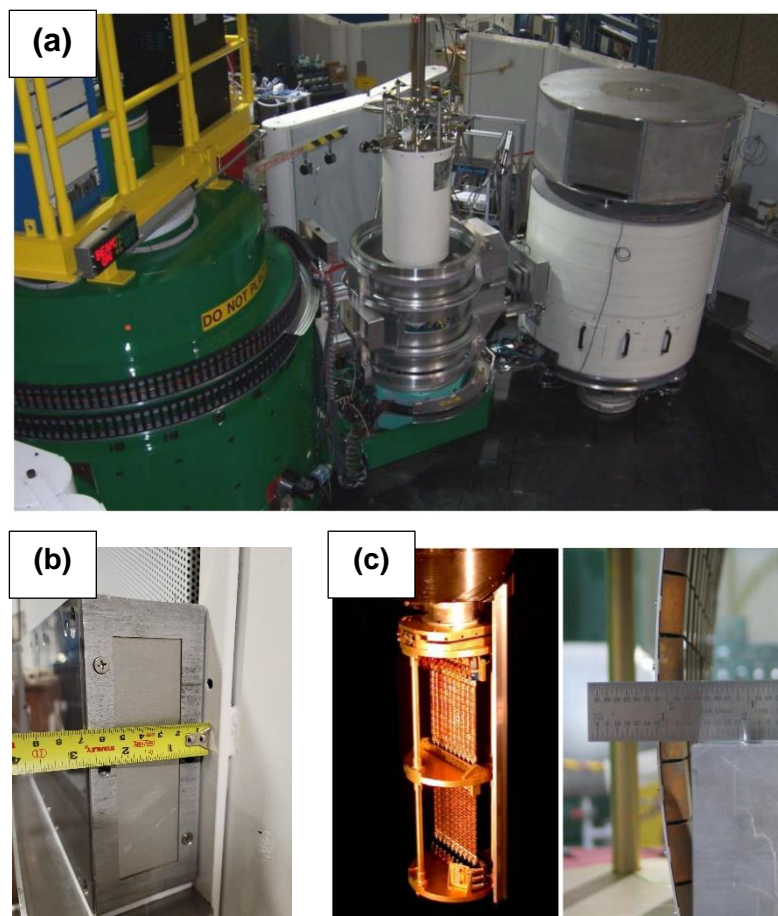


Fig. 3 (a) The BT-7 thermal triple-axis spectrometer at NCNR. The green drum contains the monochromator, in-pile PG filter, and in-pile Söller collimator, and the white drum contains the analyzer and detector systems. The sample and sample environment are in the central drum. (b) A Söller slit collimator. (c) (Left) Double stack monochromator system. (Right) Vertical focusing is achieved by bending the Al plates (and then translating the array to maintain a centered monochromator), which is done under computer control.

- **Monochromator:** BT-7 has two monochromators (Fig. 3c): Cu(220) and PG(002) – which can also be used as PG(004). Each monochromator can be used in focusing or flat mode for both the vertical and/or horizontal directions. Focusing modes increase the flux on the sample at the expense of resolution. Vertical resolution is typically relaxed on TASs (*e.g.* no vertical collimation), and BT-7 is almost always operated in vertical focusing mode to increase the flux on the sample.

- **Analyzer focusing:** The PG(002) analyzer on BT-7 can be configured in horizontal focusing or flat mode.

- **Detector modes:** The single detector after the analyzer (which is actually a cluster of three ³He detectors) is the standard mode of operation, but BT-7 also has a diffraction detector (no energy analysis), which is before the analyzer for energy integrated data collection and a position sensitive detector (PSD) which can cover an angular range in $2\theta_s$ of $\sim 5^\circ$ at once (at the elastic line). The PSD is valuable for performing survey type-scans, such as when searching for magnetic ordering wavevectors after a transition or when one needs to cover a large area of reciprocal space in a finite amount of time.

Types of diffraction scans on a TAS

Different types of scans can provide unique information about a sample in a diffraction experiment. Fig. 4 pictorially shows some of these types of scans and how they pass over

Bragg peaks in the reciprocal space of a cubic unit cell.

- Longitudinal or θ - $2\theta_s$ scans scan along a radial direction in reciprocal space defined by the scattering vector, \mathbf{Q} . For a θ - $2\theta_s$ scan, the scan variable is the scattering angle $2\theta_s$, and as the name suggests, for every step in $2\theta_s$, the sample rotation angle, θ , moves half as much.
- A θ scan (or rocking scan) keeps the scattering angle, $2\theta_s$, constant and only rotates the sample rotation angle, θ . It scans reciprocal space in a direction approximately orthogonal to that of a θ - $2\theta_s$ scan about the same point. This type of alignment scan is also used to obtain information about a crystal's mosaic, which pertains to the quality of the crystal. If the FWHM measured across a Bragg peak is resolution limited (*i.e.* it is no larger than the instrumental resolution FWHM) in a θ scan, then one can determine the upper limit of the crystal mosaic. If the FWHM is larger than the instrumental resolution, then the mosaic can be determined by increasing the mosaic FWHM in the resolution calculations until it matches the data.
- Vector scans are often used to extract correlation lengths from data. These are scans typically done along high symmetry paths in reciprocal space, such as along H , K , or L . To extract correlation lengths, you must deconvolute the Gaussian contribution to the peak intensity due to the spectrometer resolution and intrinsic

sample mosaic with that of the functional form, sometimes chosen to be a Lorentzian, that describes the short-range correlations.

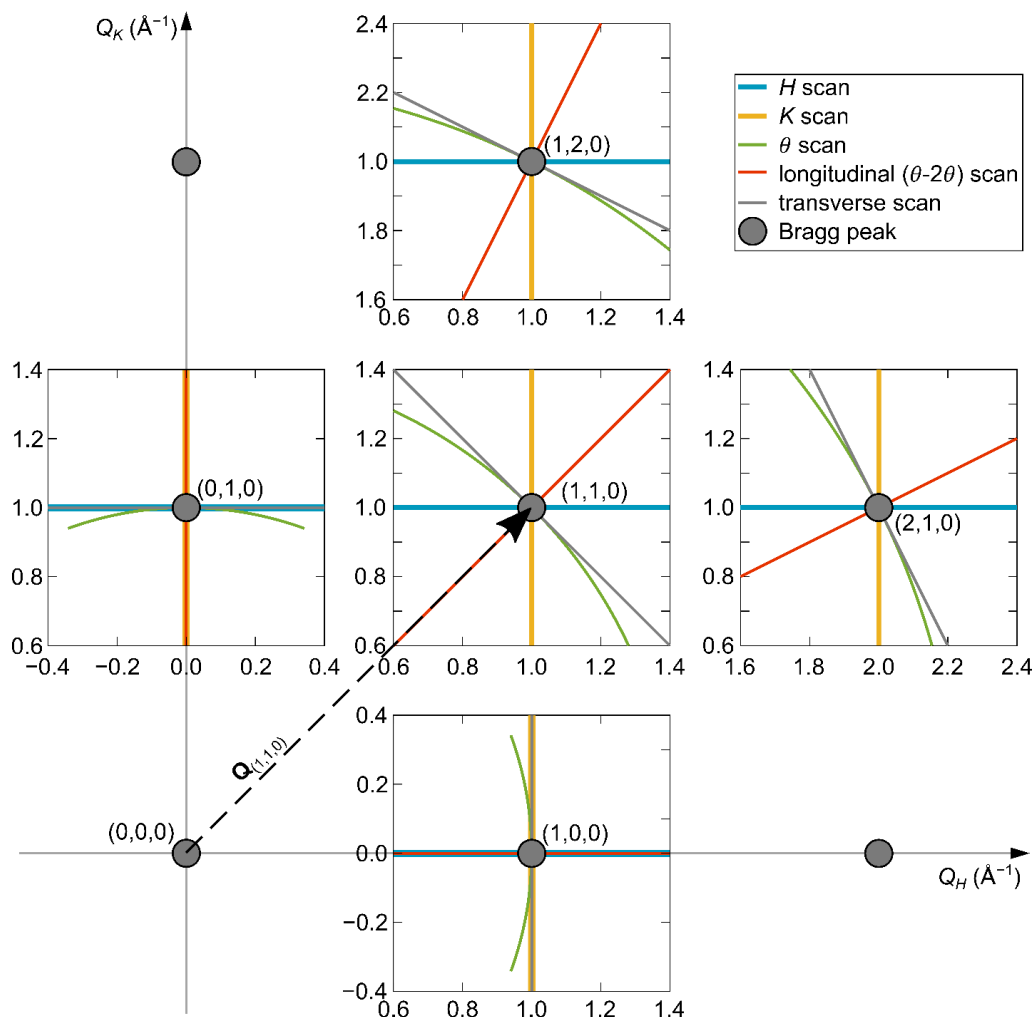


Fig. 4 Reciprocal space illustration of the $(H, K, 0)$ scattering plane of a cubic crystal with lattice parameter $a = 2\pi \text{ \AA}$, such that 1 r.l.u. = 1 \AA^{-1} . For each Bragg peak denoted, five scans are shown: H scan (blue), K scan (orange), θ scan (green), longitudinal ($\theta-2\theta_s$) scan (red), and transverse scan (grey). In the spectrometer reference frame, a longitudinal scan is always along \mathbf{Q} , and this is also the \hat{x} -axis. A transverse scan is perpendicular to \mathbf{Q} , along the \hat{y} -axis. Therefore, the reference frame axes change depending on where \mathbf{Q} is pointing in reciprocal space. Note that for small ranges, a θ scan is approximately a transverse scan.

TAS Resolution

The resolution of a TAS is determined by the resolution ellipsoid and is often calculated using a matrix method using Cooper-Nathans [6] or Popovici approximations [7]. Programs such as ResLib [8] and Takin [9] are commonly used to perform these calculations. The resolution ellipsoid spans momentum and energy space, and evaluating it correctly is essential for proper analysis of many types of TAS data, particularly when evaluating inelastic spectra. For example, the effect of the resolution ellipsoid as it passes through a dispersion curve can give the appearance of a peak at a certain (Q, E) position, when in reality, the excitation may be substantially off from that position. For diffraction, the effect of the resolution ellipsoid passing through a Bragg peak – which is a delta function – leads to the observation of peak with a functional form resembling a Gaussian. Mathematically, this shape is determined by the convolution of a delta function with the resolution function, $R(Q, E)$. If the resolution

ellipsoid is not passing through a delta function, but some other type of peak, then the observed peak shape may take on the appearance of a different functional form (*e.g.* Lorentzian). Evaluation of the resolution ellipsoid is also important if one wants to compare the intensities of different Bragg peaks, such as in a structural refinement. For this experiment, we will be comparing the same peaks to themselves as a function of temperature, so evaluating the resolution function is not as important. However, gaining an understanding of how one can modify the resolution on a TAS to obtain needed information about a sample is important to understand. In this experiment, two magnetic Bragg peaks, which are closely spaced, were tracked as a function of temperature. At high temperatures, these peaks were well-resolved with open-25°-25°-120° collimation, however, at low temperatures, they become closer, and the instrument needed to be configured with 25°-10°-10°-25° collimation to resolve them. An example of the resolution function projected onto different planes for these two collimation configurations is shown in Figs. 5-7. These figures represent an L -scan about $(1, 0, 0.25)$, which is the approximate position of the aforementioned two closely spaced magnetic Bragg peaks. The other parameters used for these calculations were those used in the experiment, as described in the Methods section.

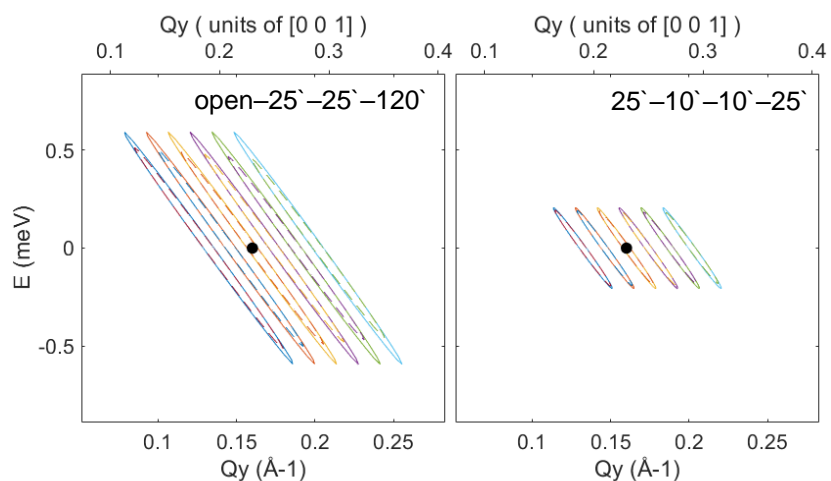


Fig. 5 Resolution ellipsoids representing different points along an L scan projected onto the $(0, 0, L)$ - E plane for two different collimation configurations. The black dot represents the center of the scan at $(1, 0, 0.25)$. Solid lines of the ellipsoid are the projection of the entire ellipsoid onto the plane, and the dashed lines are the FWHM of the ellipsoid projected onto the plane.

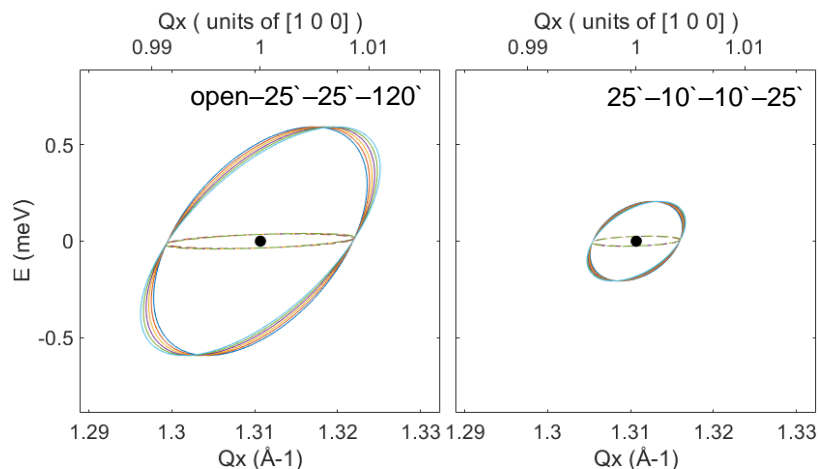


Fig. 6 Resolution ellipsoids representing different points along an L scan projected onto the $(H, 0, 0)$ - E plane for two different collimation configurations. The black dot represents the center of the scan at $(1, 0, 0.25)$. Solid lines of the ellipsoid are the projection of the entire ellipsoid onto the plane, and the dashed lines are the FWHM of the ellipsoid projected onto the plane.

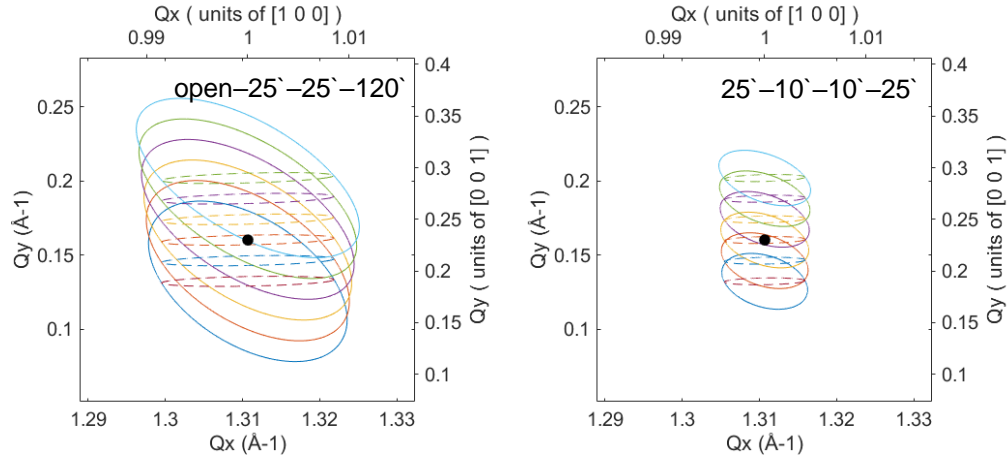
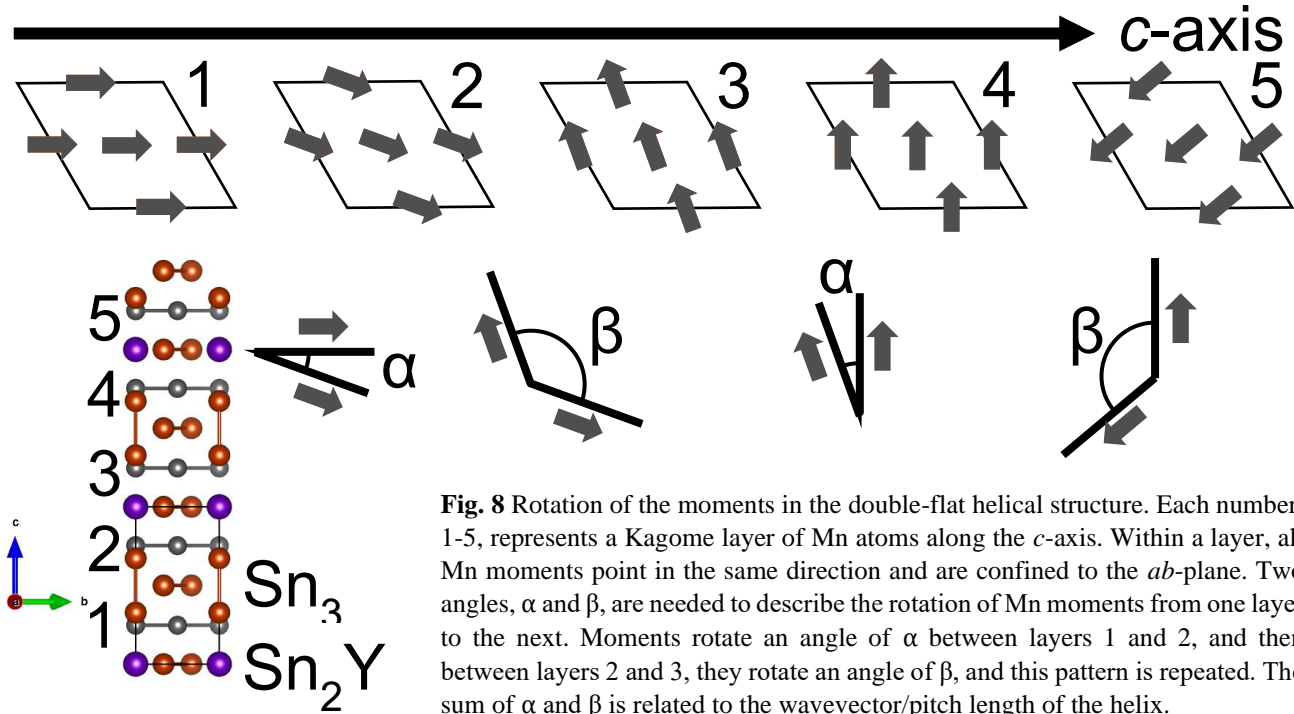


Fig. 7 Resolution ellipsoids representing different points along an L scan projected onto the $(H, 0, L)$ plane for two different collimation configurations. The black dot represents the center of the scan at $(1, 0, 0.25)$. Solid lines of the ellipsoid are the projection of the entire ellipsoid onto the plane, and the dashed lines are the FWHM of the ellipsoid projected onto the plane.

The Experiment

Scientific Background

Topologically nontrivial magnetic and electronic structures have attracted extraordinary attention in the past few years. Kagome-net magnets are one of the popular classes of these materials [10-14]. It was recently realized that highly nontrivial physics can come from noncollinear interplanar ordering between ferromagnetic (FM) Kagome planes, such as topological Hall effect in the absence of crystallographic inversion symmetry breaking [15, 16]. As opposed to antiferromagnetic (AFM) Kagome materials, for FM Kagome planes formed by the metals such as Fe or Mn, the in-plane exchange interaction is strongly FM and not magnetically frustrated but still forms characteristics of Kagome geometry: Dirac cones and flat bands [17-21]. The interesting physics comes from the fact that, by virtue of the Mermin-Wagner theorem, the FM fluctuations in the two-dimensional planes are strongly enhanced, with the magnetic order and dynamics being controlled by weak interplanar exchange interactions, which, on the contrary, can be and usually are frustrated. Thus, these materials are strongly magnetically fluctuating and provide fertile ground for interesting new phenomena. YMn_6Sn_6 is a prototype for this materials class. It forms a hexagonal $P6/mmm$ structure ($a = 5.541 \text{ \AA}$ and $c = 9.035 \text{ \AA}$) consisting of Kagome planes $[\text{Mn}_3\text{Sn}]$ separated by two inequivalent Sn_3 and Sn_2Y layers, *i.e.*, $[\text{Mn}_3\text{Sn}][\text{Sn}_3][\text{Mn}_3\text{Sn}][\text{Sn}_2\text{Y}]$ (Fig. 9a) [22, 23]. YMn_6Sn_6 is a good metal [24, 25] and, hence, is expected to have relatively long-range exchange interactions, possibly including Ruderman-Kittel-Kasuya-Yosida coupling. All Mn planes and in-plane nearest-neighbor Mn-Mn bonds are crystallographically equivalent, but the interplanar Mn-Mn bonds along the c -axis are markedly different, with a FM exchange interaction across the Sn_3 layers and AFM across the Sn_2Y layers. These are frustrated by the second-neighbor interaction across an intermediate Mn_3Sn layer (J_1 and J_3 are FM, while J_2 is AF) and result in complex magnetic behaviors [23, 24]. Below $T_N \approx 345 \text{ K}$ (Fig. 9b-d), a commensurate collinear AF structure first forms with the propagation vector $\mathbf{k} = (0, 0, \frac{1}{2})$. On cooling, an incommensurate phase quickly appears, which coexists with the commensurate phase in a narrow temperature range and becomes the only phase below $\approx 300 \text{ K}$ [23, 26]. Based on powder diffraction, the incommensurate state has been reported to have two (and even three at room temperature) nearly equal wave vectors [23], which can be described as a staggered spiral, also dubbed the “double-flat spiral,” [27] as depicted in Fig. 8. A magnetic field applied in the ab -plane induces multiple transitions seen in the magnetization and Hall resistivity [24]. An enigmatic topological Hall effect is observed at elevated temperatures, with the largest value around 245 K and a magnetic field of 4 T [25] and coincides with a transverse conical spiral magnetic structure phase.



Methods

A single crystal was oriented in the $(H, 0, L)$ scattering plane on the triple-axis neutron spectrometer BT-7. The sample was mounted in an Al can and put inside of a high-temperature, high-power closed cycle refrigerator (Fig. 2c). Elastic diffraction data were taken with $E_i = E_f = 14.7$ meV and open $-25' - 25' - 120'$ full-width-at-half-maximum (FWHM) collimators were used before and after the sample, before the analyzer, and before the detector, respectively (unless otherwise noted). A PG(002) monochromator and analyzer were used, and monochromator vertical focusing was employed. PG filters were used in-pile and after the sample to reduce $\lambda/2$ contamination. Bragg peaks were resolution limited and Gaussian in shape. Peaks were therefore fit to Gaussians with the FWHMs constrained to be that of the spectrometer resolution as determined by the program ResLib [8]. Momentum is reported in reciprocal lattice units (r.l.u.) denoted using H , K , and L , where $\mathbf{Q}[\text{\AA}^{-1}] = \left(\frac{4\pi}{\sqrt{3}a} H, \frac{4\pi}{\sqrt{3}a} K, \frac{2\pi}{c} L \right)$.

Results and Discussion

The zero-field neutron diffraction data are plotted in Fig. 9b-d. A commensurate magnetic Bragg peak is observed at the onset of long-range magnetic order, where $\mathbf{k} = (0, 0, 0.5)$ and $T_N = 345$ K, which quickly transforms into two distinct incommensurate wave vectors. These two incommensurate structures coexist from their onset to the base temperature (12 K) determined by high-resolution measurements (inset in Fig. 9b). The two wave vectors $(0, 0, k_{z,1})$ and $(0, 0, k_{z,2})$ with $k_{z,1} < k_{z,2}$ evolve smoothly with temperature along L , and $|k_{z,1} - k_{z,2}|$ decreases with cooling. The two magnetic structures stemming from $k_{z,1}$ and $k_{z,2}$ are consistent with previous reports [24, 27] (see Fig. 8) but with slightly different periodicities (Fig. 9c). The area of the magnetic Bragg peaks smoothly increases with decreasing temperature (Fig. 9d).

A simplified Hamiltonian can be used to describe the magnetic structure in zero-field:

$$H = \sum_{i,j} J_n \mathbf{n}_i \cdot \mathbf{n}_j + \sum_{i,j} J_p \mathbf{n}_i \cdot \mathbf{n}_j + K \sum_i (n_i^z)^2,$$

where J_n ($n = 1,2,3$) is the interplanar exchange as shown in Fig. 9a, J_p is the ferromagnetic nearest-neighbor intraplanar exchange as shown in Fig. 9a, and K is an easy-plane single-ion anisotropy which confines the Mn

moments to the ab -plane. The frustration from competing interplanar interactions is what leads to the formation of the double-flat spiral structure.

Currently, there is not a satisfactory explanation for the coexistence of the two, almost equivalent, wave vectors found in YMn_6Sn_6 and in some doped variants [1, 2, 23, 28]. One possibility suggested was that the magnetic structure has a non-constant rotation of the moments, and the wavevectors observed were merely harmonics of a much smaller fundamental wave vector [23]. However, recent inelastic neutron-scattering measurements show that the observed wave vectors are, in fact, the magnetic zone center [26], making the modulated structure theory obsolete. An inhomogeneous distribution of two magnetic structures, which are almost energetically identical, could also be likely. Multiple ground states have been observed in intermetallics due to off-stoichiometry, such as the fluctuating Ni concentration in $\text{CeNi}_{0.84}\text{Sn}_2$ which leads to two coexisting magnetic ground states [29], or the ground-state sensitivity to the Sn content in $\text{Ce}_3\text{Rh}_4\text{Sn}_{13}$ [30]. Most similar is the itinerant antiferromagnet, Mn_3Sn , where two helical modulations coexist over a wide temperature range [31]. The incommensurate transition

temperature and wavevector values were also shown to have a dependence on the annealing history, implying disorder may play a role in the magnetic structure [32]. However, synchrotron powder diffraction data [2] show that if chemical inhomogeneity were the root cause for the double wavevectors then there is no associated structural inhomogeneity in the form of a distribution of lattice parameters, and our neutron diffraction data show that the regions of homogeneous chemical compositions would have to be large enough to lead to long-range magnetic order (*i.e.* $>1000 \text{ \AA}$). This does not rule out macroscopic regions of varying Sn content as being responsible for the two propagation vectors and further chemical characterization on the Sn inhomogeneity across a crystal would shed more light on this possibility.

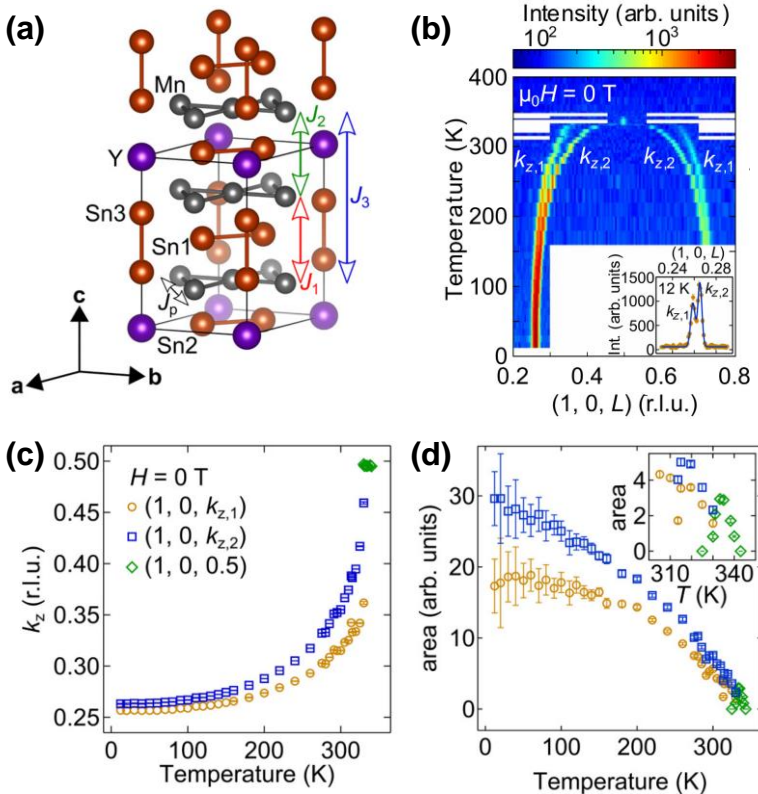


Fig. 9 (a) YMn_6Sn_6 crystal structure where the solid black lines outline a single unit cell. The basal plane Mn-Mn bonds are shown as solid grey lines between. J_p , J_1 , J_2 , and J_3 represent the most relevant Heisenberg exchange paths for the magnetic Hamiltonian. (b)-(d) Single-crystal neutron diffraction results for YMn_6Sn_6 . (b) Magnetic Bragg peaks tracked as a function of temperature. A commensurate magnetic peak at $L = 0.5$ appears between 345 K and 330 K, and the two incommensurate magnetic structures stemming from the wave vectors $k_{z,1}$ and $k_{z,2}$ appear at 330 K and persist to the base temperature measured (12 K). The inset, taken with high instrumental resolution ($25^\circ-10'-10'-25^\circ$), shows that the two wave vectors do not converge, even as they get closer with decreasing temperature. (c) and (d) are the fitted results from (b) showing the wavevector and area evolution as a function of temperature, respectively. Figures taken from Refs. [1] and [2].

Experiment Checklist

Alignment

- Mount sample (seal sample cans with Pb if going above 400 K, no stainless steel if using polarized neutrons)
- Load sample into cryostat (what kind of cryostat are you using? If high temperature – no Cd!)
- Put cryostat onto instrument via crane lift (authorized users only)
- Set the incident and final energy (typically 14.7 meV for a diffraction experiment)
- Use instrument alignment procedure to define scattering plane and tell instrument how the sample is oriented.

Configure instrument

- Scan the vertical and horizontal slits before and after the sample. This will reduce background scattering into the detector.
- Check mosaic of sample with current collimation. This is done via a sample rotation scan (shown as θ in Fig. 1 and is often called a θ scan as shown in Fig. 4) about a Bragg peak. Are there multiple peaks, or is it resolution limited? If resolution limited, are there reasons you may want to tighten the collimation (at the expense of flux)?
- Are the PG filters in? Depending on E_i , and whether you are doing diffraction or inelastic scattering, sometimes the velocity selector is a better choice for minimizing $\lambda/2$ contamination in the beam (and higher orders for the velocity selector).
- Configure the detector (PSD, single detector?)
- Check alignment a final time after all configuration is completed.

Begin data collection

- Decide if you want to start at high or low temperature
- Set up the L -scans to cover the magnetic Bragg peaks at $(1,0, L+k_z)$. How large of an L -range do you need to cover, and what step size should you take?
- Begin collecting data
- Lattice parameters change with temperature; should you also change the lattice parameter inputs on the instrument?
- Evaluate the quality of your data. Do you need to fill in temperatures? Change the instrument configuration to obtain specific information?
- Here, we changed the collimation to be tighter to collect additional data. What is the difference in the data with this new collimation versus the original collimation?

Data analysis

- Load files into DAVE
- Reduce data
- Batch fit like-data sets
- Plot data

References

- [1] N. J. Ghimire et al., *Sci. Adv.* **6**, eabe2680 (2020). <https://doi.org/10.1126/sciadv.abe2680>
- [2] R. L. Dally et al., *Phys. Rev. B* **103**, 094413 (2021). <https://doi.org/10.1103/PhysRevB.103.094413>
- [3] J. W. Lynn et al. *Journal of Research of NIST* **117**, 61-79 (2012). <http://dx.doi.org/10.6028/jres.117.002>
- [4] W. C. Chen et al., *Physica B: Condensed Matter* **397**(1-2), 168-171 (2007). <https://doi.org/10.1016/j.physb.2007.02.053>
- [5] R. M. Moon et al. *Phys. Rev.* **181**, 920 (1969). <https://doi.org/10.1103/PhysRev.181.920>
- [6] M. J. Cooper and R. Nathans. The resolution function in neutron diffractometry. I. *Acta Crystallographica*, **23**(3):357–367 (1967). <https://doi.org/10.1107/S0365110X67002816>.
- [7] M. Popovici. *Acta Crystallographica Section A*, **31**(4):507–513 (1975). <https://doi.org/10.1107/S0567739475001088>.
- [8] Andrey Zheludev. Reslib v3.4c, <https://neutron.ethz.ch/methods/reslib.html>, 2009.
- [9] Tobias Weber. Update 2.0 to “Takin: An open-source software for experiment planning, visualisation, and data analysis”, (PII: S2352711016300152). *SoftwareX*, **14**:100667, 2021. ISSN 2352-7110. <https://doi.org/10.1016/j.softx.2021.100667>.
- [10] J. Zang et al., V. Cros, A. Hoffmann, *Topology in Magnetism* (Springer, 2018).
- [11] N. Nagaosa and Y. Tokura. *Nat. Nanotechnol.* **8**, 899–911 (2013). <https://doi.org/10.1038/nnano.2013.243>
- [12] N. Nagaosa et al. *Phil. Trans. R. Soc. A* **370**, 5806–5819 (2012). <https://doi.org/10.1098/rsta.2011.0405>
- [13] B. Bradlyn et al. *Science*, **353**, aaf5037 (2016). <https://doi.org/10.1126/science.aaf5037>
- [14] N. P. Armitage et al. *Rev. Mod. Phys.* **90**, 15001 (2018). <https://doi.org/10.1103/RevModPhys.90.015001>

- [15] J. Kübler and C. Fesler. *Europhys. Lett.* **108**, 67001 (2014). <https://doi.org/10.1209/0295-5075/108/67001>
- [16] S. Nakatsuji et al. *Nature*, **527**, 212–215 (2015). <https://doi.org/10.1038/nature15723>
- [17] N. J. Ghimire and I. I. Mazin. *Nat. Mater.* **19**, 137–138 (2020). <https://doi.org/10.1038/s41563-019-0589-8>
- [18] M. Kang et al. *Nat. Mater.* **19**, 163–169 (2020). <https://doi.org/10.1038/s41563-019-0531-0>
- [19] L. Ye et al. *Nature*, **555**, 638–642 (2018). <https://doi.org/10.1038/nature25987>
- [20] E. Liu et al. *Nat. Phys.* **14**, 1125–1131 (2018). <https://doi.org/10.1038/s41567-018-0234-5>
- [21] J. X. Yin et al. *Nat. Phys.* **15**, 443–448 (2019). <https://doi.org/10.1038/s41567-019-0426-7>
- [22] C. Lefèvre et al. *J. Alloys Compd.* **361**, 40–47 (2003). [https://doi.org/10.1016/S0925-8388\(03\)00421-3](https://doi.org/10.1016/S0925-8388(03)00421-3)
- [23] G. Venturini et al. *J. Alloys Compd.* **236**, 102–110 (1996). [https://doi.org/10.1016/0925-8388\(95\)01998-7](https://doi.org/10.1016/0925-8388(95)01998-7)
- [24] K. Uhlířová, et al. *WDS'06 Proceedings of Contributed Papers Part III*, 48–53 (2006).
- [25] Q. Wang et al. *Phys. Rev. B* **103**, 014416 (2021). <https://doi.org/10.1103/PhysRevB.103.014416>
- [26] H. Zhang, et al. *Phys. Rev. B* **101**, 100405 (2020). <https://doi.org/10.1103/PhysRevB.101.100405>
- [27] E. V. Rosenfeld and N. V. Mushnikov. *Physica B* **403**, 1898–1906 (2008).
<https://doi.org/10.1016/j.physb.2007.10.220>
- [28] L. Eichenberger, et al. *J. Alloy Compd.* **695**, 286 (2017). <https://doi.org/10.1016/j.jallcom.2016.10.191>
- [29] P. Schobinger-Papamantellos, et al. *J. Phys.-Condens. Mat.* **8**, 8635 (1996). <https://doi.org/10.1088/0953-8984/8/44/014>
- [30] A. Šlebarski et al. *Phys. Rev. B* **86**, 205113 (2012). <http://dx.doi.org/10.1103/PhysRevB.86.205113>
- [31] J. W. Cable et al. *Solid State Commun.* **88**, 161 (1993). [https://doi.org/10.1016/0038-1098\(93\)90400-H](https://doi.org/10.1016/0038-1098(93)90400-H)
- [32] G. G. Marcus, Ph.D. thesis, Johns Hopkins University (2018).